Exploration of mass splitting and muon/tau mixing parameters for an eV-scale sterile neutrino with IceCube

R. Abbasi[q], M. Ackermann[bm], J. Adams[r], S. K. Agarwalla[an,1], J. A. Aguilar[l], M. Ahlers[v], J.M. Alameddine[w], N. M. Amin[ar], K. Andeen[ap], C. Argüelles[n], Y. Ashida[ba], S. Athanasiadou[bm], L. Ausborm[a], S. N. Axani[ar], X. Bai[ax], A. Balagopal V.[an], M. Baricevic[an], S. W. Barwick[ad], S. Bash[aa], V. Basu[an], R. Bay[h], J. J. Beatty[t,u], J. Becker Tjus[k,2], J. Beise[bk], C. Bellenghi[aa], C. Benning[a], S. BenZvi[az], D. Berley[s], E. Bernardini[av], D. Z. Besson[aj], E. Blaufuss[s], L. Bloom[bh], S. Blot[bm], F. Bontempo[ae], J. Y. Book Motzkin[n], C. Boscolo Meneguolo[av], S. Böser[ao], O. Botner[bk], J. Böttcher[a], J. Braun[an], B. Brinson[f], J. Brostean-Kaiser[bm], L. Brusa[a], R. T. Burley[b], D. Butterfield[an], M. A. Campana[aw], I. Caracas[ao], K. Carloni[n], J. Carpio[ah,ai], S. Chattopadhyay[an,1], N. Chau[l], Z. Chen[bd], D. Chirkin[an], S. Choi[be,bf], B. A. Clark[s], A. Coleman[bk], G. H. Collin[o], A. Connolly[t,u], J. M. Conrad[o], P. Coppin[m], R. Corley[ba], P. Correa[m], D. F. Cowen[bi,bj], P. Dave[f], C. De Clercq[m], J. J. DeLaunay[bh], D. Delgado[n], S. Deng[a], A. Desai[an], P. Desiati[an], K. D. de Vries[m], G. de Wasseige[ak], T. DeYoung[x], A. Diaz[o,4], J. C. Díaz-Vélez[an], P. Dierichs[a], M. Dittmer[aq], A. Domi[z], L. Draper[ba], H. Dujmovic[an], K. Dutta[ao], M. A. DuVernois[an], T. Ehrhardt[ao], L. Eidenschink[aa], A. Eimer[z], P. Eller[aa], E. Ellinger[bl], S. El Mentawi[a], D. Elsässer[w], R. Engel[ae,af], H. Erpenbeck[an], J. Evans[s], P. A. Evenson[ar], K. L. Fan[s], K. Fang[an], K. Farrag[p], A. R. Fazely[g], A. Fedynitch[bg], N. Feigl[j], S. Fiedlschuster[z], C. Finley[bc], L. Fischer[bm], D. Fox[bi], A. Franckowiak[k], S. Fukami[bm], P. Fürst[a], J. Gallagher[am], E. Ganster[a], A. Garcia[n], M. Garcia[ar], G. Garg[an,1], E. Genton[n,ak], L. Gerhardt[i], A. Ghadimi[bh], C. Girard-Carillo[ao], C. Glaser[bk], T. Glüsenkamp[z,bk], J. G. Gonzalez[ar], S. Goswami[ah,ai], A. Granados[x], D. Grant[x], S. J. Gray[s], O. Gries[a], S. Griffin[an], S. Griswold[az], K. M. Groth[v], C. Günther[a], P. Gutjahr[w], C. Ha[bb], C. Haack[z], A. Hallgren[bk], L. Halve[a], F. Halzen[an], H. Hamdaoui[bd], M. Ha Minh[aa], M. Handt[a], K. Hanson[an], J. Hardin[o], A. A. Harnisch[x], P. Hatch[ag], A. Haungs[ae], J. Häußler[a], K. Helbing[bl], J. Hellrung[k], J. Hermannsgabner[a], L. Heuermann[a], N. Heyer[bk], S. Hickford[bl], A. Hidvegi[bc], C. Hill[p], G. C. Hill[b], K. D. Hoffman[s], S. Hori[an], K. Hoshina[an,3], M. Hostert[n], W. Hou[ae], T. Huber[ae], K. Hultqvist[bc], M. Hünnefeld[w], R. Hussain[an], K. Hymon[w], A. Ishihara[p], W. Iwakiri[p], M. Jacquart[an], O. Janik[z], M. Jansson[bc], G. S. Japaridze[e], M. Jeong[ba], M. Jin[n], B. J. P. Jones[d], N. Kamp[n], D. Kang[ae], W. Kang[be], X. Kang[aw], A. Kappes[aq], D. Kappesser[ao], L. Kardum[w], T. Karg[bm], M. Karl[aa], A. Karle[an], A. Katil[y], U. Katz[z], M. Kauer[an], J. L. Kelley[an], M. Khanal[ba], A. Khatee Zathul[an], A. Kheirandish[ah,ai], J. Kiryluk[bd], S. R. Klein[h,i], A. Kochocki[x], R. Koirala[ar], H. Kolanoski[j], T. Kontrimas[aa], L. Köpke[ao], C. Kopper[z], D. J. Koskinen[v], P. Koundal[ar], M. Kovacevich[aw], M. Kowalski[j,bm], T. Kozynets[v], J. Krishnamoorthi[an,1], K. Kruiswijk[ak], E. Krupczak[x], A. Kumar[bm], E. Kun[k], N. Kurahashi[aw], N. Lad[bm], C. Lagunas Gualda[bm], M. Lamoureux[ak], M. J. Larson[s], S. Latseva[a], F. Lauber[bl], J. P. Lazar[ak], J. W. Lee[be], K. Leonard DeHolton[bj], A. Leszczyńska[ar], J. Liao[f], M. Lincetto[k], Y. T. Liu[bj], M. Liubarska[y], E. Lohfink[ao], C. Love[aw], C. J. Lozano Mariscal[aq], L. Lu[an], F. Lucarelli[ab], W. Luszczak[t,u], Y. Lyu[h,i], J. Madsen[an], E. Magnus[m], K. B. M. Mahn[x], Y. Makino[an], E. Manao[aa], S. Mancina[an,av], W. Marie Sainte[an], I. C. Mariş[l], S. Marka[at], Z. Marka[at], M. Marsee[bh], I. Martinez-Soler[n], R. Maruyama[as], F. Mayhew[x], F. McNally[al], J. V. Mead[v], K. Meagher[an], S. Mechbal[bm], A. Medina[u], M. Meier[p], Y. Merckx[m], L. Merten[k], J. Micallef[x], J. Mitchell[g], T. Montaruli[ab], R. W. Moore[y], Y. Morii[p], R. Morse[an], M. Moulai[an], T. Mukherjee[ae], R. Naab[bm], R. Nagai[p], M. Nakos[an], U. Naumann[bl], J. Necker[bm], A. Negi[d], L. Neste[bc], M. Neumann[aq], H. Niederhausen[x], M. U. Nisa[x], K. Noda[p], A. Noell[a], A. Novikov[ar], A. Obertacke Pollmann[p], V. O'Dell[an], B. Oeyen[ac], A. Olivas[s], R. Orsoe[aa], J. Osborn[an], E. O'Sullivan[bk], H. Pandya[ar], N. Park[ag], G. K. Parker[d], E. N. Paudel[ar], L. Paul[ax], C. Pérez de los Heros[bk], T. Pernice[bm], J. Peterson[an], S. Philippen[a], A. Pizzuto[an], M. Plum[ax], A. Pontén[bk], Y. Popovych[ao], M. Prado Rodriguez[an], B. Pries[x], R. Procter-Murphy[s], G. T. Przybylski[i], C. Raab[ak], J. Rack-Helleis[ao], M. Ravn[bk], K. Rawlins[c], Z. Rechav[an], A. Rehman[ar], P. Reichherzer[k], E. Resconi[aa], S. Reusch[bm], W. Rhode[w], B. Riedel[an], A. Rifaie[a], E. J. Roberts[b], S. Robertson[h,i], S. Rodan[be,bf], G. Roellinghoff[be], M. Rongen[z], A. Rosted[p], C. Rott[ba,be], T. Ruhe[w], L. Ruohan[aa], D. Ryckbosch[ac], I. Safa[an], J. Saffer[af], D. Salazar-Gallegos[x], P. Sampathkumar[ae], A. Sandrock[bl], M. Santander[bh], S. Sarkar[y], S. Sarkar[au], J. Savelberg[a], P. Savina[an], P. Schaile[aa], M. Schaufel[a], H. Schieler[ae], S. Schindler[z], B. Schlüter[aq], F. Schlüter[l], N. Schmeisser[bl], T. Schmidt[s], J. Schneider[z], F. G. Schröder[ae,ar], L. Schumacher[z], S. Sclafani[s], D. Seckel[ar], M. Seikh[aj], M. Seo[be], S. Seunarine[ay], P. Sevle Myhr[ak], R. Shah[aw], S. Shefali[af], N. Shimizu[p], M. Silva[an], B. Skrzypek[h], B. Smithers[d], R. Snihur[an], J. Soedingrekso[w], A. Søgaard[v], D. Soldin[ba], P. Soldin[a], G. Sommani[k], C. Spannfellner[aa], G. M. Spiczak[ay], C. Spiering[bm], M. Stamatikos[u], T. Stanev[ar], T. Stezelberger[i], T. Stürwald[bl], T. Stuttard[v], G. W. Sullivan[s], I. Taboada[f], S. Ter-Antonyan[g], A. Terliuk[aa], M. Thiesmeyer[a], W. G. Thompson[n], J. Thwaites[an], S. Tilav[ar], K. Tollefson[x], C. Tönnis[be], S. Toscano[l], D. Tosi[an], A. Trettin[bm], R. Turcotte[ae], J. P. Twagirayezu[x], M. A. Unland Elorrieta[aq], A. K. Upadhyay[an,1], K. Upshaw[g], A. Vaidyanathan[ap], N. Valtonen-Mattila[bk], J. Vandenbroucke[an], N. van Eijndhoven[m], D. Vannerom[o], J. van Santen[bm], J. Vara[aq], F. Varsi[af], J. Veitch-Michaelis[an], M. Venugopal[ae], M. Vereecken[ak], S. Verpoest[ar], D. Veske[at], A. Vijai[s], C. Walck[bc], A. Wang[f], C. Weaver[x], P. Weigel[o], A. Weindl[ae], J. Weldert[bj], A. Y. Wen[n], C. Wendt[an], J. Werthebach[w], M. Weyrauch[ae], N. Whitehorn[x], C. H.

---

[1] also at Institute of Physics, Sachivalaya Marg, Sainik School Post, Bhubaneswar 751005, India

[2] also at Department of Space, Earth and Environment, Chalmers University of Technology, 412 96 Gothenburg, Sweden

[3] also at Earthquake Research Institute, University of Tokyo, Bunkyo, Tokyo 113-0032, Japan

[4] now at Division of Physics, Mathematics and Astronomy, California Institute of Technology, Pasadena, CA, 91125, USA

arXiv:2406.00905v2 [hep-ex] 21 Oct 2024

Wiebusch[a], D. R. Williams[bh], L. Witthaus[w], A. Wolf[a], M. Wolf[aa], G. Wrede[z], X. W. Xu[g], J. P. Yanez[y], E. Yildizci[an], S. Yoshida[p], R. Young[aj], S. Yu[ba], T. Yuan[an], Z. Zhang[bd], P. Zhelnin[n], P. Zilberman[an], M. Zimmerman[an]

[a]*III. Physikalisches Institut, RWTH Aachen University, D-52056 Aachen, Germany*
[b]*Department of Physics, University of Adelaide, Adelaide, 5005, Australia*
[c]*Dept. of Physics and Astronomy, University of Alaska Anchorage, 3211 Providence Dr., Anchorage, AK 99508, USA*
[d]*Dept. of Physics, University of Texas at Arlington, 502 Yates St., Science Hall Rm 108, Box 19059, Arlington, TX 76019, USA*
[e]*CTSPS, Clark-Atlanta University, Atlanta, GA 30314, USA*
[f]*School of Physics and Center for Relativistic Astrophysics, Georgia Institute of Technology, Atlanta, GA 30332, USA*
[g]*Dept. of Physics, Southern University, Baton Rouge, LA 70813, USA*
[h]*Dept. of Physics, University of California, Berkeley, CA 94720, USA*
[i]*Lawrence Berkeley National Laboratory, Berkeley, CA 94720, USA*
[j]*Institut für Physik, Humboldt-Universität zu Berlin, D-12489 Berlin, Germany*
[k]*Fakultät für Physik & Astronomie, Ruhr-Universität Bochum, D-44780 Bochum, Germany*
[l]*Université Libre de Bruxelles, Science Faculty CP230, B-1050 Brussels, Belgium*
[m]*Vrije Universiteit Brussel (VUB), Dienst ELEM, B-1050 Brussels, Belgium*
[n]*Department of Physics and Laboratory for Particle Physics and Cosmology, Harvard University, Cambridge, MA 02138, USA*
[o]*Dept. of Physics, Massachusetts Institute of Technology, Cambridge, MA 02139, USA*
[p]*Dept. of Physics and The International Center for Hadron Astrophysics, Chiba University, Chiba 263-8522, Japan*
[q]*Department of Physics, Loyola University Chicago, Chicago, IL 60660, USA*
[r]*Dept. of Physics and Astronomy, University of Canterbury, Private Bag 4800, Christchurch, New Zealand*
[s]*Dept. of Physics, University of Maryland, College Park, MD 20742, USA*
[t]*Dept. of Astronomy, Ohio State University, Columbus, OH 43210, USA*
[u]*Dept. of Physics and Center for Cosmology and Astro-Particle Physics, Ohio State University, Columbus, OH 43210, USA*
[v]*Niels Bohr Institute, University of Copenhagen, DK-2100 Copenhagen, Denmark*
[w]*Dept. of Physics, TU Dortmund University, D-44221 Dortmund, Germany*
[x]*Dept. of Physics and Astronomy, Michigan State University, East Lansing, MI 48824, USA*
[y]*Dept. of Physics, University of Alberta, Edmonton, Alberta, T6G 2E1, Canada*
[z]*Erlangen Centre for Astroparticle Physics, Friedrich-Alexander-Universität Erlangen-Nürnberg, D-91058 Erlangen, Germany*
[aa]*Physik-department, Technische Universität München, D-85748 Garching, Germany*
[ab]*Département de physique nucléaire et corpusculaire, Université de Genève, CH-1211 Genève, Switzerland*
[ac]*Dept. of Physics and Astronomy, University of Gent, B-9000 Gent, Belgium*
[ad]*Dept. of Physics and Astronomy, University of California, Irvine, CA 92697, USA*
[ae]*Karlsruhe Institute of Technology, Institute for Astroparticle Physics, D-76021 Karlsruhe, Germany*
[af]*Karlsruhe Institute of Technology, Institute of Experimental Particle Physics, D-76021 Karlsruhe, Germany*
[ag]*Dept. of Physics, Engineering Physics, and Astronomy, Queen's University, Kingston, ON K7L 3N6, Canada*
[ah]*Department of Physics & Astronomy, University of Nevada, Las Vegas, NV 89154, USA*
[ai]*Nevada Center for Astrophysics, University of Nevada, Las Vegas, NV 89154, USA*
[aj]*Dept. of Physics and Astronomy, University of Kansas, Lawrence, KS 66045, USA*
[ak]*Centre for Cosmology, Particle Physics and Phenomenology - CP3, Université catholique de Louvain, Louvain-la-Neuve, Belgium*
[al]*Department of Physics, Mercer University, Macon, GA 31207-0001, USA*
[am]*Dept. of Astronomy, University of Wisconsin—Madison, Madison, WI 53706, USA*
[an]*Dept. of Physics and Wisconsin IceCube Particle Astrophysics Center, University of Wisconsin—Madison, Madison, WI 53706, USA*
[ao]*Institute of Physics, University of Mainz, Staudinger Weg 7, D-55099 Mainz, Germany*
[ap]*Department of Physics, Marquette University, Milwaukee, WI 53201, USA*
[aq]*Institut für Kernphysik, Westfälische Wilhelms-Universität Münster, D-48149 Münster, Germany*
[ar]*Bartol Research Institute and Dept. of Physics and Astronomy, University of Delaware, Newark, DE 19716, USA*
[as]*Dept. of Physics, Yale University, New Haven, CT 06520, USA*
[at]*Columbia Astrophysics and Nevis Laboratories, Columbia University, New York, NY 10027, USA*
[au]*Dept. of Physics, University of Oxford, Parks Road, Oxford OX1 3PU, United Kingdom*
[av]*Dipartimento di Fisica e Astronomia Galileo Galilei, Università Degli Studi di Padova, I-35122 Padova PD, Italy*
[aw]*Dept. of Physics, Drexel University, 3141 Chestnut Street, Philadelphia, PA 19104, USA*
[ax]*Physics Department, South Dakota School of Mines and Technology, Rapid City, SD 57701, USA*
[ay]*Dept. of Physics, University of Wisconsin, River Falls, WI 54022, USA*
[az]*Dept. of Physics and Astronomy, University of Rochester, Rochester, NY 14627, USA*
[ba]*Department of Physics and Astronomy, University of Utah, Salt Lake City, UT 84112, USA*
[bb]*Dept. of Physics, Chung-Ang University, Seoul 06974, Republic of Korea*
[bc]*Oskar Klein Centre and Dept. of Physics, Stockholm University, SE-10691 Stockholm, Sweden*
[bd]*Dept. of Physics and Astronomy, Stony Brook University, Stony Brook, NY 11794-3800, USA*
[be]*Dept. of Physics, Sungkyunkwan University, Suwon 16419, Republic of Korea*
[bf]*Institute of Basic Science, Sungkyunkwan University, Suwon 16419, Republic of Korea*
[bg]*Institute of Physics, Academia Sinica, Taipei, 11529, Taiwan*
[bh]*Dept. of Physics and Astronomy, University of Alabama, Tuscaloosa, AL 35487, USA*
[bi]*Dept. of Astronomy and Astrophysics, Pennsylvania State University, University Park, PA 16802, USA*
[bj]*Dept. of Physics, Pennsylvania State University, University Park, PA 16802, USA*
[bk]*Dept. of Physics and Astronomy, Uppsala University, Box 516, SE-75120 Uppsala, Sweden*
[bl]*Dept. of Physics, University of Wuppertal, D-42119 Wuppertal, Germany*
[bm]*Deutsches Elektronen-Synchrotron DESY, Platanenallee 6, D-15738 Zeuthen, Germany*

Abstract

We present the first three-parameter fit to a 3+1 sterile neutrino model using 7.634 years of data from the IceCube Neutrino Observatory on $\nu_\mu + \bar{\nu}_\mu$ charged-current interactions in the energy range 500–9976 GeV. Our analysis is sensitive to the mass-squared splitting between the heaviest and lightest mass state (Δm_{41}^2), the mixing matrix element connecting muon flavor to the fourth mass state ($|U_{\mu 4}|^2$), and the element connecting tau flavor to the fourth mass state ($|U_{\tau 4}|^2$). Predicted propagation effects in matter enhance the signature through a resonance as atmospheric neutrinos from the Northern Hemisphere traverse the Earth to the IceCube detector at the South Pole. The remaining sterile neutrino matrix elements are left fixed, with $|U_{e4}|^2 = 0$ and $\delta_{14} = 0$, as they have a negligible effect, and $\delta_{24} = \pi$ is set to give the most conservative limits. The result is consistent with the no-sterile neutrino hypothesis with a probability of 4.3%. Profiling the likelihood of each parameter yields the 90% confidence levels: $2.4\,\text{eV}^2 < \Delta m_{41}^2 < 9.6\,\text{eV}^2$, $0.0081 < |U_{\mu 4}|^2 < 0.10$, and $|U_{\tau 4}|^2 < 0.035$, which narrows the allowed parameter-space for $|U_{\tau 4}|^2$. However, the primary result of this analysis is the first map of the 3+1 parameter space exploring the interdependence of Δm_{41}^2, $|U_{\mu 4}|^2$, and $|U_{\tau 4}|^2$.

Keywords: atmospheric neutrino IceCube TeV oscillation sterile

1. Introduction

Over the past quarter century, anomalies observed in short-baseline neutrino experiments have been studied within the context of vacuum neutrino oscillations involving the three known flavors (ν_e, ν_μ and ν_τ) and an additional hypothetical 'sterile neutrino' (ν_s) that has no left-handed weak interactions. This "3+1" model predicts three related signatures: $\nu_\mu \rightarrow \nu_e$ appearance, ν_e disappearance, and ν_μ disappearance. While supporting evidence for anomalous oscillations have been found in short-baseline $\nu_\mu \rightarrow \nu_e$ appearance [1, 2] and ν_e disappearance [3, 4] experiments, no evidence has been found for ν_μ disappearance [5, 6]. Further, other $\nu_\mu \rightarrow \nu_e$ appearance [7, 8] and ν_e disappearance [9–11] experiments fail to observe anomalous oscillations, and inconsistencies between all datasets lead to tensions within the "3+1" model [12–15].

Neutrino telescopes offer an alternative method to probe for the ν_μ disappearance signal using atmospheric muon-flavor neutrino interactions at TeV-scale energies. For these events, theoretical studies of 3+1 models predict, along with vacuum oscillations, a resonance signature induced by matter propagation effects on the $\bar{\nu}_\mu$ flux traversing the Earth which cause a deficit of "up-going" events [16–21]. While the resonance signature will appear in the $\bar{\nu}_\mu$ flux, current gigaton-scale high energy ($\gtrsim 1$ TeV) neutrino telescopes cannot efficiently differentiate between a ν_μ and $\bar{\nu}_\mu$ interaction, and so measure the combined ($\nu_\mu + \bar{\nu}_\mu$) rate. Further, due to sparse instrumentation, the oscillation signature is highly smeared in reconstructed energy. However, the matter resonance effect may be sufficiently strong that neutrino telescopes still have the sensitivity to explore a wide range of 3+1 model parameter space. Among existing neutrino telescopes, the IceCube Neutrino Observatory, a cubic-kilometer neutrino detector buried 1.5–2.5 km beneath the South Pole in the Antarctic glacier [22], is both the largest and longest running experiment. Therefore, it is the most promising in this search for new physics.

2. Muon flavor disappearance in IceCube and the 3+1 model

The 3+1 model parameterization introduces a new singlet state ν_s and a new mass state ν_4. The flavor mixing is described by expanding the PMNS 3-flavor mixing matrix to a 4×4 mixing matrix U_{3+1} that connects the flavor states (ν_e, ν_μ, ν_τ, and ν_s) to the mass states (ν_1, ν_2, ν_3, and ν_4):

$$U_{3+1} = \begin{pmatrix} U_{e1} & U_{e2} & U_{e3} & U_{e4} \\ U_{\mu 1} & U_{\mu 2} & U_{\mu 3} & U_{\mu 4} \\ U_{\tau 1} & U_{\tau 2} & U_{\tau 3} & U_{\tau 4} \\ U_{s1} & U_{s2} & U_{s3} & U_{s4} \end{pmatrix}. \tag{1}$$

The matrix elements can be parameterized in terms of three new mixing angles (θ_{14}, θ_{24} and θ_{34}) and two new CP-violating parameters (δ_{14} and δ_{24}). Within this multi-parameter model, three parameters, $|U_{\mu 4}|^2$, $|U_{\tau 4}|^2$, and Δm_{41}^2, will most affect IceCube's TeV-scale muon-neutrino disappearance search. This paper focuses on those parameters and sets the other parameters to $|U_{e4}|^2 = 0$, $\delta_{14} = 0$, and $\delta_{24} = \pi$.

Setting $|U_{e4}|^2$ (or, equivalently, the mixing angle θ_{14}) to zero is well-justified since the atmospheric neutrino flux in the TeV energy range has an electron-flavor content of less than 10% [23, 24]. As a result, contributions to muon flavor events involving $|U_{e4}|^2$, which would come mainly from $\nu_e \rightarrow \nu_\mu$ oscillations, can be safely neglected [25–27]. With $|U_{e4}|^2 = 0$, the CP-violation term δ_{14} no longer contributes and is arbitrarily set to zero.

In a matter-enhanced disappearance search, δ_{24} is expected to produce a minimal effect in the analysis for two reasons. First, at energies above 500 GeV, the lower bound of this analysis, δ_{24} is sub-leading to the other parameters [27]. Second, non-zero δ_{24} weakens the disappearance of the ν_μ flux while simultaneously strengthening the disappearance of the $\bar{\nu}_\mu$ flux, partially canceling out the effect to the overall $\nu_\mu + \bar{\nu}_\mu$ flux. However, since the ν_μ cross-section is larger than the $\bar{\nu}_\mu$ cross-section, the overall $\nu_\mu + \bar{\nu}_\mu$ event rate will slightly increase (i.e., the disappearance will weaken) with increasing δ_{24}. Therefore, the most conservative choice is to fix δ_{24} to the value that produces the

weakest oscillation effect, $\delta_{24} = \pi$, which our sensitivity studies confirm.

With the above assumptions, IceCube TeV-scale muon-flavor disappearance analyses depend upon two mixing matrix elements related to two mixing angles:

$$|U_{\mu 4}|^2 = \sin^2 \theta_{24} \qquad (2)$$
$$|U_{\tau 4}|^2 = \sin^2 \theta_{34} \cos^2 \theta_{24}. \qquad (3)$$

Terms depending on $|U_{\tau 4}|^2$ have a smaller effect than those that depend on $|U_{\mu 4}|^2$. Therefore, previous matter-enhanced Ice-Cube analyses have assumed $\theta_{34} = |U_{\tau 4}|^2 = 0$ [28–30], reducing the model to only two parameters and improving the speed of fits to data. However, as the precision of the IceCube data set has been enhanced through increased statistics (a factor of 15 between Ref. [28] and Refs. [29, 30]) and better estimation of systematic uncertainties, the effect of a non-zero $|U_{\tau 4}|^2$ must now be studied.

Figure 1 presents 'oscillograms' illustrating how the atmospheric neutrino flux changes for some representative sterile neutrino mixing parameters. The left plot shows $\bar{\nu}_\mu$ disappearance as a function of true neutrino energy and direction, assuming a particular value of Δm_{41}^2 and $|U_{\mu 4}|^2$, while keeping $|U_{\tau 4}|^2 = 0$. The neutrino's direction serves as a proxy for the distance and amount of matter it traversed between creation and arrival at the IceCube detector. The direction is given by $\cos(\theta_z)$, where θ_z is the zenith angle. In these coordinates, $\cos(\theta_z) = -1$ corresponds to "up-going" events that traverse the Earth's diameter, while $\cos(\theta_z) = 0$ are events coming from the horizon. For the chosen values of Δm_{41}^2 and $|U_{\mu 4}|^2$, the sterile-induced signature is the resonant deficit localized in direction and energy at $\cos(\theta_z) \approx -1$ and $E_\nu \sim 10^4$ GeV. These disappearing neutrinos primarily oscillate into the sterile ν_s state. The middle plot shows how the oscillogram changes further when introducing a non-zero $|U_{\tau 4}|^2$. The $\bar{\nu}_\mu$ resonant disappearance is smeared lower in energy and becomes more up-going. In this scenario, there is also significant $\bar{\nu}_\mu \to \bar{\nu}_\tau$ appearance that further modifies the observed signal, as seen in the right plot.

As seen in Table 1, the present limits on $|U_{\tau 4}|^2$ apply in restricted Δm_{41}^2 ranges where rapid oscillations cause the experiments to be insensitive to this parameter, reducing the analyses to two-parameter fits in $|U_{\mu 4}|^2$ and $|U_{\tau 4}|^2$, which are correlated. This motivates the present study to *simultaneously* improve our knowledge of all three parameters, Δm_{41}^2, $|U_{\mu 4}|^2$, and $|U_{\tau 4}|^2$. This letter will present frequentist and Bayesian results that characterize these parameters.

3. Event selection and analysis

The analysis considers a muon deficit within the combined atmospheric and astrophysical muon-flavor neutrino and antineutrino fluxes. The selection is dominated by the atmospheric flux that is initiated through cosmic ray interactions with the Earth's atmosphere. To generate the atmospheric flux, IceCube uses the `MCEq` software [23], which takes a specific

Experiment [Ref.]	$|U_{\tau 4}|^2$ at 90% (99%) CL	Δm_{41}^2
IceCube-DeepCore [31]	< 0.15	> 1 eV^2
Super-Kamiokande [32]	< 0.18 (0.23)	> 0.1 eV^2
T2K [33]	< 0.50	> 0.1 eV^2
ANTARES [34]	< 0.40 (0.68)	> 0.5 eV^2

Table 1: Summary of previous limits on $|U_{\tau 4}|^2$ at the 90% (99%, if available) confidence level and the applicable Δm_{41}^2 range where the predicted oscillation is sufficiently fast to be effectively averaged over. In these analyses there is a dependence between $|U_{\tau 4}|^2$ and $|U_{\mu 4}|^2$ values, thus the applicable $|U_{\mu 4}|^2$ parameter space for these constraints is also limited.

cosmic ray model as input and produces the resulting flux, calculated according to a particular hadronic interaction model. We use the Hillas-Gaisser 2012 H3a cosmic ray model [35] with the SIBYLL 2.3c hadronic interaction model [36]. The flux further depends on the Earth's atmospheric density profile, obtained from data from the AIRS instrument on NASA's Aqua satellite [37].

The prompt atmospheric component originates from the decays of charmed mesons produced by cosmic ray interactions. These heavier hadrons decay before substantial energy loss, resulting in a harder spectrum than the 'conventional' flux discussed above. We use the expected flux derived in Ref. [38] as input. A prompt atmospheric component has yet to be identified in IceCube, with a $1\,\sigma$ upper limit found at a factor of ~5 greater than the baseline model used [39]. Within the energy range of interest for this analysis, the prompt component is expected to contribute less than 1% to the overall event rate.

The astrophysical neutrino flux was first measured by IceCube [40, 41, 39], and is fit by an isotropic, falling power-law spectrum:

$$\frac{dN_\nu}{dE} = \Phi_{\text{astro}} \times \left(\frac{E_\nu}{100\,\text{TeV}} \right)^{-\gamma_{\text{astro}}}, \qquad (4)$$

where Φ_{astro} is the normalization for a single neutrino flavor and charge (i.e., either ν or $\bar{\nu}$) and γ_{astro} is the spectral index. This analysis is not sensitive to the details of the spectral shape of the astrophysical neutrino flux. However, Φ_{astro} and γ_{astro} are included as nuisance parameters with central values and correlated priors chosen according to a combined fit of the results of Refs. [39, 42, 43]. The central values used are $\Phi_{\text{astro}} = 0.787 \times 10^{-18}\,\text{GeV}^{-1}\,\text{sr}^{-1}\,\text{s}^{-1}\,\text{cm}^{-2}$ and $\gamma_{\text{astro}} = 2.5$. The analysis assumes equal flavor content ($\nu_e{:}\nu_\mu{:}\nu_\tau {::} 1{:}1{:}1$) and equal $\nu/\bar{\nu}$ flux.

In a 3+1 model, the resonance occurs as the neutrinos propagate through the Earth's matter. The effects of the parameters, $|U_{\mu 4}|^2$, $|U_{\tau 4}|^2$, and Δm_{41}^2, are calculated using the neutrino propagation software `nuSQuIDS` [44], which adopts the neutrino mixing matrix [45] and the interaction cross-section [46] relevant at these energies to model coherent and incoherent interactions, including tau neutrino regeneration [47].

An example of the effect that the existence of a sterile neutrino would have on the oscillations was discussed earlier and shown in Figure 1 as a function of true neutrino energy E_ν and true neutrino direction $\cos(\theta_z)$. The Earth's density as a function of radius is taken to follow the PREM model [48].

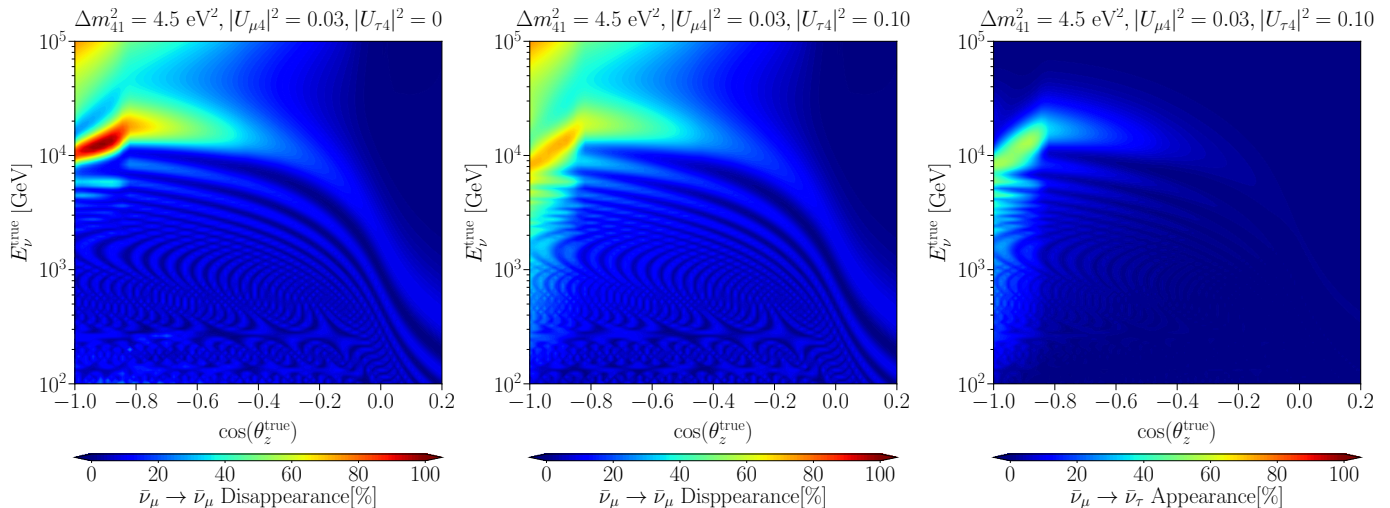Neutrino interactions are detected using the IceCube Neu-

4

Figure 1: **Left:** This oscillogram shows $\bar{\nu}_\mu$ disappearance while propagating through the Earth, as a function of true neutrino energy and direction, assuming $\Delta m^2_{41} = 4.5\,\text{eV}^2$, $|U_{\mu4}|^2 = 0.03$ and $|U_{\tau4}|^2 = 0.0$. **Center:** This oscillogram demonstrates how the $\bar{\nu}_\mu$ disappearance changes with the non-zero value of $|U_{\tau4}|^2 = 0.1$. **Right:** This oscillogram shows the $\bar{\nu}_\mu \to \bar{\nu}_\tau$ appearance once $|U_{\tau4}|^2$ has been set to the non-zero value.

trino detector located at the geographic South Pole. For a detailed description of the apparatus, see Ref. [22]. Upgoing charged-current (CC) muon (anti)neutrino interactions that occur below and within the IceCube detector are identified via muon tracks observed in the detector. Tracks are reconstructed [49, 50] based on emitted Cherenkov light collected by 'Digital Optical Modules' (DOMs) [51] arranged in two hexagonal arrays. The main array comprises 78 strings, each carrying 60 DOMs with 17 m spacing, separated by 125 m. The Deep-Core [52] subdetector, an 8-string array with variable string-spacing between 42 m and 72 m and vertical DOM separation of 7 m, is also used in this analysis.

This analysis follows recent TeV-scale IceCube 3+1 analyses [29, 30, 53] in the event selection and reconstruction procedure. A total of 305,735 track-like events, selected to have reconstructed energy between 500 GeV and 9976 GeV, were collected over a live time of 7.634 years between May 2011 and May 2019. Tracks are selected so their reconstructed direction is within $-1 \leq \cos(\theta_z) \leq 0$, where $\cos(\theta_z) = -1$ corresponds to upgoing tracks and $\cos(\theta_z) = 0$ to events at the horizon. Even at the horizon, the matter traversed corresponds to 124 km of water-equivalent overburden at the top of the detector. Hence, upgoing tracks are likely to originate from muon-neutrino interactions near the detector rather than from atmospheric muons penetrating through the Earth. The selected sample is therefore expected to be composed of >99.9% ν_μ +$\bar{\nu}_\mu$ CC events [30]. Since the event selection includes events that originate outside of the detector as well as tracks that exit the detector, the muon energy resolution is $\sigma\left(\log_{10}(E_\mu)\right) \sim 0.5$. However, the combination of long track lengths of $O(1\,\text{km})$ and large detector size allows direction reconstruction to better than $1°$ [49, 54]. Of the events in the selection, we expect ~20% of events to originate from the bedrock, which lies approximately 362 m below the bottom of the detector.

Simulated neutrino interaction points are chosen and weighted using the `LeptonInjector` and `LeptonWeighter`

software [55], respectively. For different sterile neutrino models, `LeptonWeighter` reweights each simulated event by the oscillated neutrino flux outputted by `nuSQuIDS`. After selecting a neutrino interaction point, the secondary products are propagated through the rock and ice using the `PROPOSAL` software [56].

The $\nu_\tau/\bar{\nu}_\tau$ CC interactions will create τ^-/τ^+ that can decay leptonically to μ^-/μ^+, producing tracks in the sample. While the direct production of tau-neutrinos in the dominant atmospheric flux is very low, nonzero $|U_{\tau4}|^2$, i.e. nonzero θ_{34} (Eq. 3), allows for non-negligible $\bar{\nu}_\mu \to \bar{\nu}_\tau$ appearance above 500 GeV. Tau neutrinos also contribute to the astrophysical flux. Past matter-induced IceCube sterile neutrino analyses [29, 30] did not simulate tau-flavor contributions. For this analysis, $\nu_\tau/\bar{\nu}_\tau$ simulations were produced and `PROPOSAL` was modified to account for the τ polarization when decaying into a μ. A separate ν_τ interaction cross-section is not needed, as mass effects at energies far above the τ-lepton mass are negligible. For the sterile hypothesis parameters used in Figure 1, $\bar{\nu}_\mu \to \bar{\nu}_\tau$ appearance contributes an additional 2% of tracks in the upward direction, while contributing negligible events from the horizon.

The systematic uncertainties adopted in this analysis have been detailed in previous IceCube analyses [29, 30, 53]. The list appears in Table 2. The eighteen parameters fall into four categories: conventional atmospheric flux parameters, detector parameters, astrophysical neutrino flux parameters, and cross-section parameters. In the analysis, different values for the systematic parameters modify the weights for the simulated events. No uncertainties were placed on the Standard Model neutrino oscillation parameters.

The majority of these nuisance parameters concern the conventional atmospheric flux. Two parameters quantify the uncertainty in the cosmic ray flux. The first is an overall normalization factor N, while the second is a spectral shape correction

Systematic Parameter	Prior	Pull(σ)
Conventional Flux Parameters		
Normalization (N)	1.00 ± 0.40	0.51
Spectral shift ($\Delta\gamma_{\text{conv.}}$)	0.00 ± 0.25	0.44
Atm. Density	0.00 ± 1.00	-0.03
WP	0.00 ± 0.40	-0.13
WM	0.00 ± 0.40	-0.06
YP	0.00 ± 0.30	-0.35
YM	0.00 ± 0.30	-0.04
ZP	0.00 ± 0.12	-0.02
ZM	0.00 ± 0.12	0.01
Detector Parameters		
DOM Efficiency	0.97 ± 0.10	-0.02
Hole Ice (p_2)	-1.00 ± 10.00	-0.23
Ice Gradient 0	$0.00 \pm 1.00^*$	0.10
Ice Gradient 1	$0.00 \pm 1.00^*$	0.09
Astrophysics Parameters		
Normalization ($\Phi_{\text{astro.}}$)	$0.787 \pm 0.36^*$	0.99
Spectral shape ($\Delta\gamma_{\text{astro.}}$)	$2.50 \pm 0.36^*$	0.92
Cross Section Parameters		
Cross Section σ_{ν_μ}	1.00 ± 0.03	-0.00
Cross Section $\sigma_{\bar{\nu}_\mu}$	1.000 ± 0.075	0.02
Kaon Energy Loss σ_{KA}	0.00 ± 1.00	-0.13

Table 2: The list of systematic uncertainties used in this analysis. The second column provides their central values and prior widths, while the third column gives the best-fit value pulls from the central value. Asterisks indicate correlated priors. Atmospheric flux parameterizations involving WP through ZM are defined in Ref. [30].

term $\Delta\gamma_{\text{conv.}}$ applied as

$$\Phi(E_\nu; \Delta\gamma_{\text{conv.}}) = N\, \Phi_{\text{conv.}}(E_\nu)\left(\frac{E_\nu}{2.2\,\text{TeV}}\right)^{-\Delta\gamma_{\text{conv.}}}, \qquad (5)$$

where $\Phi_{\text{conv.}}$ is the nominal conventional neutrino flux and $\Delta\gamma_{\text{conv.}}$ is centered at zero. The only significant change from previous analyses [29, 30, 53] was to extend the prior on the cosmic ray spectral slope width $\Delta\gamma_{\text{conv.}}$ from 0.03 to 0.25, to accommodate deviations from the Hillas-Gaisser 2012 H3a cosmic ray model spectrum recently observed in the rigidity region of interest $E = 10^3\,\text{GeV} - 10^4\,\text{GeV}$ [57].

Another six conventional flux nuisance parameters vary the meson production rate in the hadronic interactions between cosmic rays and the Earth's atmosphere. The six parameters correspond to the uncertainties for kaon productions in different sectors of the interaction kinematic phase space, as described in Ref. [58]. The six parameters are labeled in Table 2 as WP, WM, YP, YM, ZP, and ZM. The first letter for each label (W, Y, Z) corresponds to the kinematic phase space where the uncertainty is applied (see Fig. 2 in Ref. [58]), and the second letter (M, P) defines whether that uncertainty is applied to the negatively (M) or positively (P) charged meson. Of the remaining uncertainties in Ref. [58], they either correspond to low energy interactions (<30 GeV) or to pion interactions. They are found

to be negligible for this analysis, since the neutrino flux above $O(100\,\text{GeV})$ is primarily produced through kaon decays [30].

A final conventional flux parameter quantifies uncertainties in the Earth's atmospheric density profile.

Detector uncertainties account for another four nuisance parameters. The first uncertainty is the DOM efficiency, which accounts for uncertainties both in the DOM response as well as uncertainties in bulk ice properties that uniformly affect the detection of photons throughout the detector. The second uncertainty pertains to the refrozen ice immediately surrounding the DOM strings. This parameter, labeled "Hole Ice (p_2)" in Table 2, is more thoroughly described in Ref. [30].

Two further parameters are implemented for the uncertainties and non-uniformities of the bulk ice of the Antarctic glacier. As described in Ref. [59], the depth dependence of the bulk ice property can be expressed in terms of a Fourier decomposition. The effect of these Fourier modes can be parameterized by two basis functions, and the amplitudes of these basis functions are implemented as systematic parameters [30]. In Table 2, they are labeled as "Ice Gradient 0" and "Ice Gradient 1."

Two nuisance parameters are included to vary the normalization and spectral shape of the astrophysical neutrino flux given in Equation (4).

Finally, three cross-section nuisance parameters are included. Two are for uncertainties in neutrino and antineutrino interactions, and one last parameter is for kaon interaction cross-section uncertainties as they propagate through the Earth's atmosphere.

Plots showing how the expected event rate changes as a function of the systematic parameters are included in Appendix A.

Two analyses were conducted: a frequentist parameter estimation and a Bayesian model comparison. In both cases, the physics parameters are sampled in a three-dimensional grid in (Δm_{41}^2, $|U_{\mu 4}|^2$, $|U_{\tau 4}|^2$)-space. The parameter bounds and step sizes are:

$$\Delta m_{41}^2 \in [0.1, 50]\,\text{eV}^2 \text{ in steps of 0.1 in } \log_{10}(\Delta m_{41}^2),$$
$$|U_{\mu 4}|^2 \in [0.001, 0.5] \text{ in steps of 0.1 in } \log_{10}(|U_{\mu 4}|^2),$$
$$|U_{\tau 4}|^2 \in [0.001, 0.5] \text{ in steps of 0.2 in } \log_{10}(|U_{\tau 4}|^2).$$

The abstract and conclusion state the frequentist result.

The data are binned in two dimensions: reconstructed cosine of the zenith angle, $\cos(\theta_z)$, and $\log_{10}$ of the reconstructed muon energy, E. The reconstructed zenith is bounded between $\cos(\theta_z) = -1$ and $\cos(\theta_z) = 0$, with 20 bins of width $\Delta\cos(\theta_z) = 0.05$. The reconstructed muon energy is bounded between $500\,\text{GeV}$ and $9976\,\text{GeV}$, in 13 bins of width $\Delta\log_{10}(E/\text{GeV}) = 0.1$.

A likelihood is constructed

$$\mathcal{L}(\vec{\theta}, \vec{\theta}_\eta) = \mathcal{L}_{\text{eff}}(\vec{\theta}, \vec{\theta}_\eta)\Pi(\vec{\theta}_\eta), \qquad (6)$$

where $\mathcal{L}(\vec{\theta}, \vec{\theta}_\eta)$ is the likelihood as a function of the fitted physics parameters $\vec{\theta} = \{\Delta m_{41}^2, |U_{\mu 4}|^2, |U_{\tau 4}|^2\}$ and systematic parameters $\vec{\theta}_\eta$. $\mathcal{L}_{\text{eff}}$ is a modified Poisson distribution to account for limited Monte Carlo statistics in estimating an expected

event rate [60]. Systematic parameters are incorporated by factoring in a prior likelihood for each parameter, $\Pi(\vec{\theta}_\eta)$, assuming a normal distribution with a given central value and width.

For the frequentist analysis, the systematic uncertainties are accounted for by using the profile likelihood at each tested physics point

$$\mathcal{L}_{\text{profile}}(\vec{\theta}) = \max_{\vec{\theta}_\eta} \mathcal{L}(\vec{\theta}, \vec{\theta}_\eta)\Pi(\vec{\theta}_\eta) \tag{7}$$

To construct confidence regions, we use the test statistic

$$\text{TS}(\vec{\theta}) = -2\Delta \log \mathcal{L}_{\text{profile}}(\vec{\theta}) \tag{8}$$

$$= -2(\log \mathcal{L}_{\text{profile}}(\vec{\theta}) - \log \mathcal{L}_{\text{profile}}(\hat{\vec{\theta}})), \tag{9}$$

where $\hat{\vec{\theta}}$ is the physics parameter point that maximizes $\mathcal{L}_{\text{profile}}$.

We also perform a Bayesian analysis, where we calculate the Bayesian 'evidence' at each physics point

$$\mathcal{E}(\vec{\theta}) = \int d\vec{\theta}_\eta \mathcal{L}(\vec{\theta}, \vec{\theta}_\eta)\Pi(\vec{\theta}_\eta), \tag{10}$$

and compare it to the evidence of the null model. The ratio between the evidence at some physics parameter point and the evidence at the null gives the Bayes factor

$$\mathcal{K}(\vec{\theta}) = \frac{\mathcal{E}(\vec{\theta} = \text{Null})}{\mathcal{E}(\vec{\theta})}, \tag{11}$$

which quantifies the preference for the null model over the alternative model. The integral in Equation (10) is calculated using the `MultiNest` algorithm [61].

To test our event selection and reconstruction, we compare our selected events with model expectations. Figure 2 shows the observed events in reconstructed energy (top) and reconstructed direction (bottom) versus the no-sterile model, shown in blue. When the data are collapsed to a single dimension the analysis loses sensitivity to the expected sterile signal, therefore providing a test of the predicted event rate without biasing the physics results. Figure 2 shows, in orange, the expected distribution from the best-fit sterile model discussed in the next section. As a goodness-of-fit test, when we run 2000 pseudo-experiments for this best-fit sterile model, we find that the 1D data distributions fall within expectation for the energy distribution with a p-value of 31%, and for the zenith distribution with a p-value of 39%.

4. Results and discussion

For the frequentist analysis, the best-fit point is found at $\Delta m_{41}^2 = 5.0\,\text{eV}^2$, $|U_{\mu4}|^2 = 0.032$, and $|U_{\tau4}|^2 = 0.010$. The 99%, 95%, and 90% confidence level (CL) regions of the fit are shown in Figure 3, assuming Wilks' theorem and three degrees of freedom for a subset of the $|U_{\tau4}|^2$ range sampled. In addition, the 99% CL median sensitivity is shown, calculated using 300 pseudo-experiments assuming the no-sterile hypothesis. The colored bands show where the middle 68.27% and 95.45% of
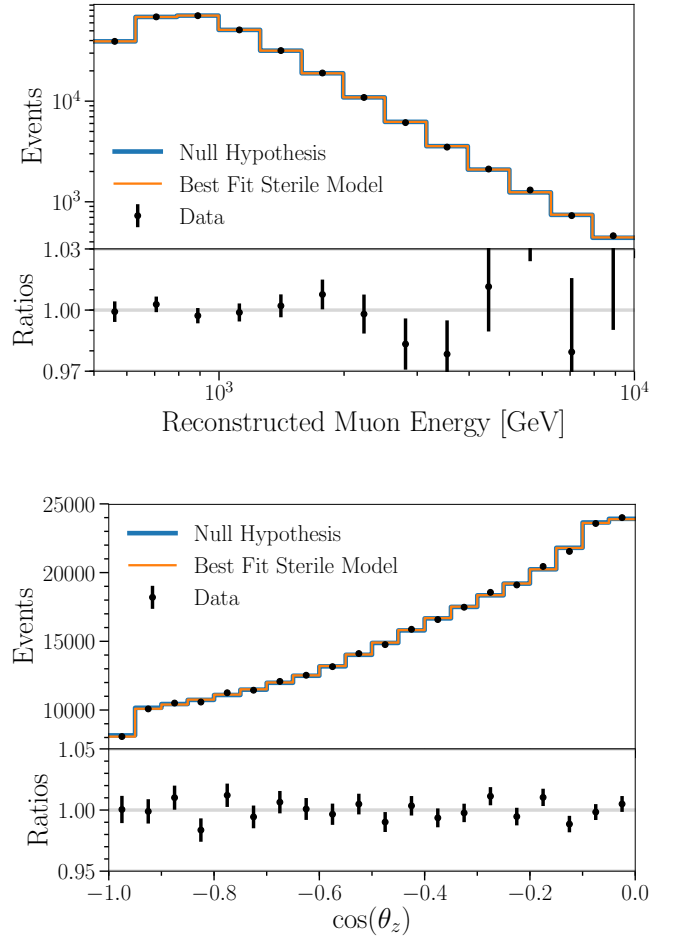

Figure 2: The 1D distribution of events selected as a function of reconstructed energy (top) and direction (bottom). Overlaid with the data are the expected distributions from the no-sterile null model (blue) and the best-fit sterile neutrino model (orange). The data points include error bars, which are too small to be observed. The ratio of the data to the best-fit model expectation is also presented.

the simulated 99% CLs lie. The expected $\bar{\nu}_\mu \rightarrow \bar{\nu}_\mu$ disappearance and $\bar{\nu}_\mu \rightarrow \bar{\nu}_\tau$ appearance oscillograms for the best-fit point can be found in Appendix B.

As a goodness-of-fit test, pseudo-experiments were run with the best-fit parameters injected as the true hypothesis. For each of these pseudo-experiments, the likelihood at the injected point $\mathcal{L}_{\text{profile}}(\vec{\theta}_{\text{injected}})$ was calculated to obtain a distribution with which to compare the observed likelihood at the best-fit point. This comparison finds that the observed data are within expectation, with a p-value of 87%. A similar exercise, with the null model as the injected and fitted parameter point, gives a p-value of 75%.

The best-fit nuisance parameters are all within 1σ of their associated nominal values, as listed in the third column of Table 2. This can be indicative of an overestimation of the systematic priors.

Figure 4 is helpful in understanding the best-fit 3+1 model. The left plot shows the bin-by-bin ratios between the predicted
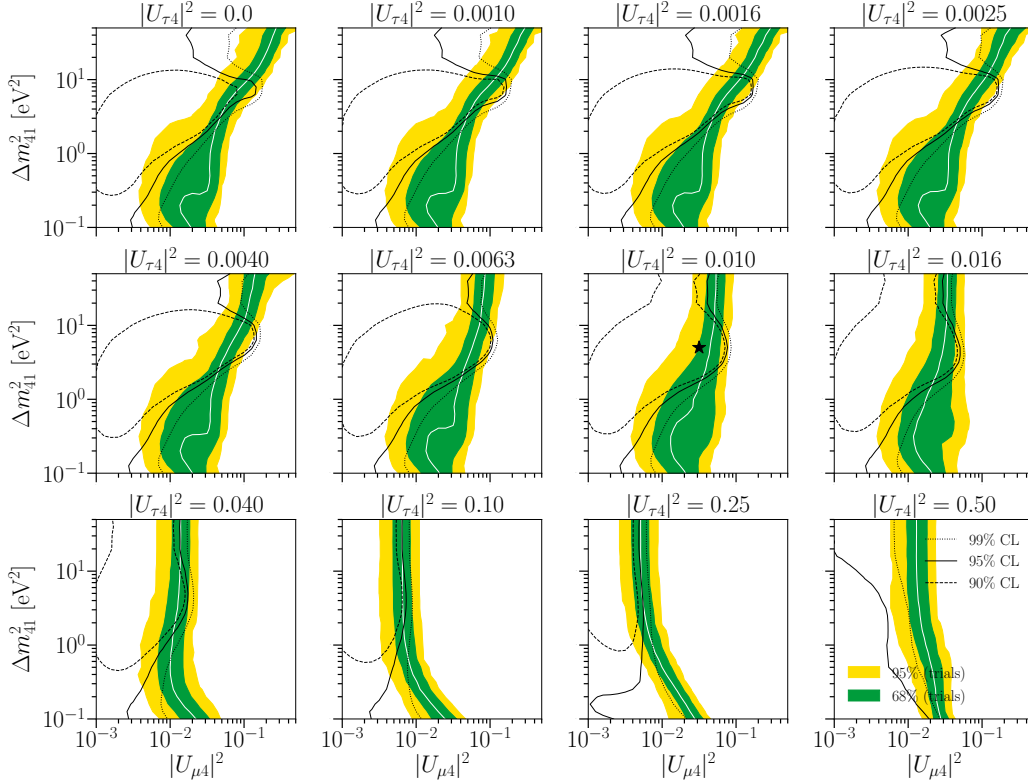
Figure 3: The 99% (dotted lines), 95% (solid lines), and 90% (dashed lines) CL regions for a selection of $|U_{\tau 4}|^2$ values tested, where the best-fit is marked with the black star ($\bigstar$). The contours are drawn assuming Wilks' theorem with three degrees of freedom as this is a three-dimensional fit. The assumption of Wilks' theorem results in the null hypothesis being allowed within the 95% CL. Pseudo-experiments, on the other hand, show that the sterile hypothesis is preferred over the null at 4.3%. The colored bands show where the middle 68.27% (green) and 95.45% (yellow) of simulated 99% CLs for no signal lie.

event rates at the best-fit point and at the null hypothesis. One can think of this prediction as the oscillogram smeared by uncertainties but without statistical variations expected in data. The characteristic deficit at low $\cos\theta_z$ that one associates with the resonance in a non-zero $|U_{\tau 4}|^2$ model is evident. An arc that results from the L/E dependence of vacuum oscillations, which appears in all 3+1 models, can be observed at higher values of $\cos\theta_z$.

In the proceeding plots in Figure 4, we show pulls, where we define the pull of model N relative to model M as

$$\text{Pull}(N; M) = \frac{E(N) - E(M)}{\sqrt{E(M)}}, \tag{12}$$

where $E(N)$ is the expected event rate for model N. We can also measure the pull of the data D relative to a model so that $E(D)$ in the above equation is the measured event rate.

The middle plot in Figure 4 presents the predicted pull, bin-by-bin, between the null hypothesis and the best-fit hypothesis, emphasizing the bins that have the most statistical power in distinguishing the two. The right plot shows the difference between the absolute values of the pull of the data from either hypothesis, i.e., |Pull(data; best fit)| − |Pull(data; null)|. If we think of |Pull(data; N)| as a measure of the disagreement of the data from model N, then |Pull(data; best fit)| − |Pull(data; null)| highlights (in red) which bins have better agreement with the best-fit model compared to the null model. These bins are most strongly contributing to the test statistic $-2\Delta\log\mathcal{L}$.

The test statistic found at the best-fit versus the no-sterile hypotheses point gives a $-2\Delta\log\mathcal{L} = 6.9$. According to Wilks' theorem, with three degrees of freedom, the sterile hypothesis is favored over the null hypothesis with a probability of 7.5%. However, pseudo-experiments can be conducted in order to calculate a more accurate probability without relying on Wilks' theorem. With 1000 simulations, we obtain a preference for the sterile hypothesis over the null hypothesis of 4.3%, corresponding to a 2σ significance, as reported in the abstract and conclusion.

We can compare this to the result of a traditional 3+1 fit that assumes $|U_{\tau 4}|^2 = 0$. If we restrict $|U_{\tau 4}|^2 = 0$, we find the best-fit to be $\Delta m_{41}^2 = 5.0\,\text{eV}^2$ and $|U_{\mu 4}|^2 = 0.025$, with $-2\Delta\log\mathcal{L} = 4.7$. Assuming Wilks' theorem, this gives a consistency with the null hypothesis of 10%, in agreement with pseudo-experiment simulations, and corresponding to 1.7σ significance.

Accurately determining preferred regions without relying on Wilks' Theorem by using pseudo-experiments, as in Figure 3, would require hundreds of simulations to be run at each sampled physics parameter point; this is computationally unfeasible. Instead, we ran simulations at a selection of parameter points, described in Appendix C. This study found that assuming Wilks' theorem with three degrees of freedom provides similar or more conservative exclusions at the 99%, 95% and 90% CL. To reduce the computational overheads, we draw these confidence regions assuming Wilks' theorem.
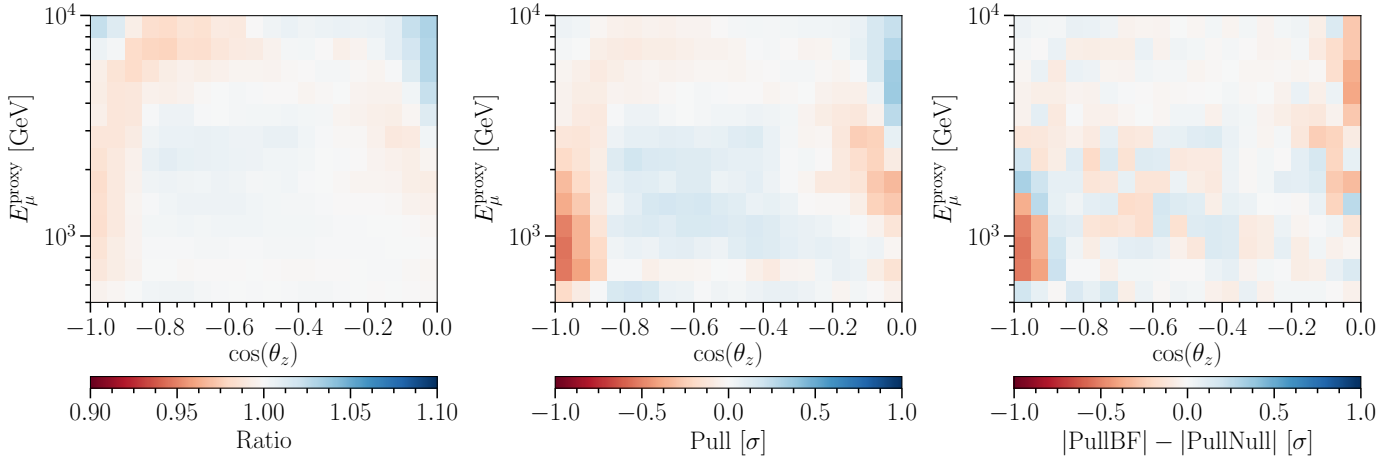
8

Figure 4: **Left:** Ratio of the expected event rate for the best-fit hypothesis over the null hypothesis, bin-by-bin, in the $\log_{10}(E)$ versus $\cos(\theta_z)$ plane. **Middle:** Statistical pulls of the best-fit predicted event rate compared to the null expectation, bin-by-bin. **Right:** Difference between the absolute value of the pull of the data from the null hypothesis, and the absolute value of the pull of the data from the best-fit hypothesis. Red bins indicate where the data are in better agreement with the best-fit hypothesis, than with the null hypothesis; these are the bins driving the fit to the best-fit hypothesis point.

To compare to other experiments, we profile over Δm_{41}^2 and compare contours in the $(|U_{\mu4}|^2, |U_{\tau4}|^2)$ parameter space. We show these comparisons in Figure 5. The 90% CL contours are shown in the lower left panel. We see that, in this 2D space, the present analysis gives complementary coverage to other experiments. The upper left and far right panels in Figure 5 show the $-2\Delta \log \mathcal{L}$ distribution when $(\Delta m_{41}^2, |U_{\tau4}|^2)$ and $(\Delta m_{41}^2, |U_{\mu4}|^2)$, respectively, have been minimized over. The grey lines show the $-2\Delta \log \mathcal{L}$ critical values for the 90% and 99% CL at one degree of freedom. For $|U_{\mu4}|^2$ and $|U_{\tau4}|^2$, the 90% (99%) CL ranges for our analysis are

$$0.0081 < |U_{\mu4}|^2 < 0.10 \; (|U_{\mu4}|^2 < 0.16)$$
$$|U_{\tau4}|^2 < 0.035 \; (|U_{\tau4}|^2 < 0.48).$$

One sees that the $-2\Delta \log \mathcal{L}$ distribution is relatively shallow. Thus, the best-fit is not strongly preferred over a wide range of values in matrix element space. Therefore, while some matrix element combinations are disfavored by other experiments, other parameter combinations remain viable.

The best-fit Bayes factor, relative to the null, is $\log_{10}(\mathcal{K}) = -1.4$ at $\Delta m_{41}^2 = 5.0\,\text{eV}^2$, $|U_{\mu4}|^2 = 0.040$, and $|U_{\tau4}|^2 = 0.0063$. With our sampling, this point is adjacent to the best-fit frequentist point. Following Jeffreys' scale [62], this corresponds to a "strong" preference over the null model. Figure 6 shows the Bayesian fit across a subset of sampled values of $|U_{\tau4}|^2$. The black star indicates the point with the greatest evidence.

The Bayesian and frequentist fits have different interpretations. Bayesian credible regions indicate our expectation that the model parameters are at a given value. Frequentist confidence regions are constructed to have a specified prior probability (the confidence level) of including the true parameter values. A summary comparing the results of the Bayesian and frequentist fits can be found in Table 3.

IceCube does not expect a substantial increase in statistical strength in the near future because another decade would be required to double the data set; nevertheless, future improve-

Fit Param.	Frequentist	Bayesian
Δm_{41}^2	$5.0\,\text{eV}^2$	$5.0\,\text{eV}^2$
$|U_{\mu4}|^2$	0.032	0.040
$|U_{\tau4}|^2$	0.010	0.0063
	$-2\Delta \log \mathcal{L} = 6.9 \; (p = 4.3\%)$	$\log_{10} \mathcal{K} = -1.4$

Table 3: Summary of the three-parameter-fit results. The results from the frequentist and Bayesian studies identify consistent parameter regions of interest.

ments to the analysis are possible. The IceCube Upgrade [63] that will come online in the next few years is focused on increasing detector efficiency at energies below that used in this analysis. While this upgrade will improve the understanding of the ice properties, the events it can detect will not lie in the energy range of interest for this specific analysis. Therefore, near-future improvements to this study need to focus on the expansion of the data set, such as the inclusion of cascade event signatures [64] and improved event reconstruction in the relevant energy range by, for example, separating events that begin within the detector from events that start outside of the detector.

5. Conclusion

This paper has presented the first sterile-neutrino analysis that fits simultaneously for Δm_{41}^2, $|U_{\mu4}|^2$, and $|U_{\tau4}|^2$ in a 3+1 sterile model. Our study uses 305,735 IceCube muon-track events, originating from ν_μ and ν_τ CC interactions, produced below and within the detector with energies between 500 GeV and 9976 GeV. The frequentist best-fit parameter point is at $\Delta m_{41}^2 = 5.0\,\text{eV}^2$, $|U_{\mu4}|^2 = 0.032$, $|U_{\tau4}|^2 = 0.01$, and preferred over the null hypothesis (three-neutrino) with a probability of 4.3%. The Bayesian result identifies preferred regions localized on parameter values consistent with the frequentist confidence limits, demonstrating a consistent picture.
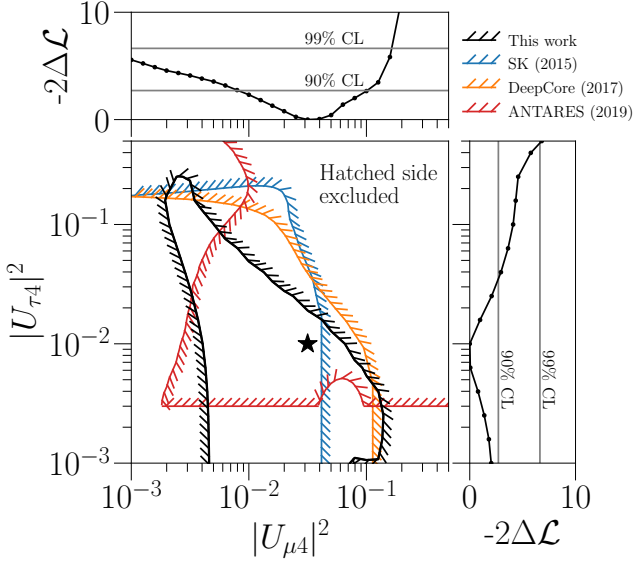
9

Figure 5: Comparison of the 90% CL contour of this analysis to Super-Kamiokande (SK) [32], IceCube-DeepCore (DeepCore) [31], and ANTARES [34]. Since other experiments do not perform a 3D fit over (Δm_{41}^2, $|U_{\mu 4}|^2$, $|U_{\tau 4}|^2$), results are profiled over Δm_{41}^2 to allow the comparison (bottom left). The hatched lines indicate the area which is excluded by the respective experiment. For ANTARES, the horizontal line at $|U_{\tau 4}|^2 = 0.003$ indicates the lower bound of that analysis. The top (right) plot shows our test statistic distribution when all parameters but $|U_{\mu 4}|^2$ ($|U_{\tau 4}|^2$) have been profiled over. The relatively shallow $-2\Delta \log \mathcal{L}$ distributions indicate the best-fit point (star) is not strongly favored within the wide allowed range. The two gray lines mark the 90% and 99% critical values for Wilks' theorem in one dimension.

As seen in Figure 5, our result is consistent with other experiments when the analysis is reduced to two parameters, $|U_{\mu 4}|^2$ and $|U_{\tau 4}|^2$, through profiling in order to enable comparison. However, information is lost when one reduces to these parameters because the full 3+1 model predicts dependence on Δm_{41}^2 in the range of 1 to 10 eV^2, as can be seen in the three-parameter fits presented in Figure 3. Hence, experiments that by design average over this range of Δm_{41}^2 lack essential sensitivity. Our result, therefore, illustrates the importance of expanding to three parameters fits for Δm_{41}^2, $|U_{\mu 4}|^2$, and $|U_{\tau 4}|^2$ to test the 3+1 model, particularly for experiments that do not suffer fast oscillations for Δm_{41}^2 in the 1–10 eV^2 range.

Acknowledgements

References

[1] C. Athanassopoulos, et al., Evidence for nu(mu) —> nu(e) neutrino oscillations from LSND, Phys. Rev. Lett. 81 (1998) 1774–1777. arXiv: nucl-ex/9709006, doi:10.1103/PhysRevLett.81.1774.

[2] A. A. Aguilar-Arevalo, et al., Updated MiniBooNE neutrino oscillation results with increased data and new background studies, Phys. Rev. D 103 (5) (2021) 052002. arXiv:2006.16883, doi:10.1103/PhysRevD.103.052002.

[3] V. V. Barinov, et al., Results from the Baksan Experiment on Sterile Transitions (BEST), Phys. Rev. Lett. 128 (23) (2022) 232501. arXiv:2109.11482, doi:10.1103/PhysRevLett.128.232501.

[4] G. Mention, M. Fechner, T. Lasserre, T. A. Mueller, D. Lhuillier, M. Cribier, A. Letourneau, The Reactor Antineutrino Anomaly, Phys. Rev. D 83 (2011) 073006. arXiv:1101.2755, doi:10.1103/PhysRevD.83.073006.

[5] P. Adamson, et al., Search for sterile neutrinos in MINOS and MINOS+ using a two-detector fit, Phys. Rev. Lett. 122 (9) (2019) 091803. arXiv:1710.06488, doi:10.1103/PhysRevLett.122.091803.

[6] K. B. M. Mahn, et al., Dual baseline search for muon neutrino disappearance at 0.5eV^2 < Δm^2 < 40eV^2, Phys. Rev. D 85 (2012) 032007. arXiv:1106.5685, doi:10.1103/PhysRevD.85.032007.

[7] B. Armbruster, et al., Upper limits for neutrino oscillations $\bar{\nu}_\mu \to \bar{\nu}_e$ from muon decay at rest, Phys. Rev. D 65 (2002) 112001. arXiv:hep-ex/0203021, doi:10.1103/PhysRevD.65.112001.

[8] P. Abratenko, et al., Search for an Excess of Electron Neutrino Interactions in MicroBooNE Using Multiple Final-State Topologies, Phys. Rev.
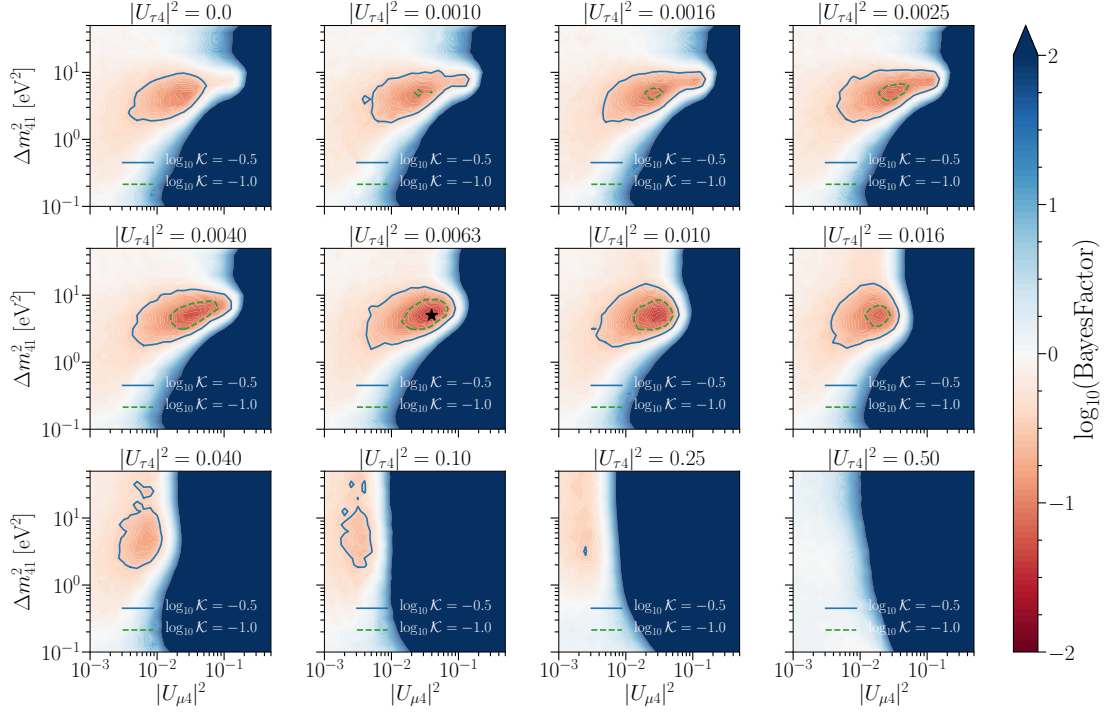
Figure 6: The Bayes Factor for a selection of $|U_{\tau4}|^2$ values tested. The Bayes Factor at each point is calculated with respect to the null model. The point with the most significant Bayes Factor is marked with the black star (★).

Lett. 128 (24) (2022) 241801. arXiv:2110.14054, doi:10.1103/PhysRevLett.128.241801.

[9] M. Andriamirado, et al., Improved short-baseline neutrino oscillation search and energy spectrum measurement with the PROSPECT experiment at HFIR, Phys. Rev. D 103 (3) (2021) 032001. arXiv:2006.11210, doi:10.1103/PhysRevD.103.032001.

[10] Z. Atif, et al., Search for sterile neutrino oscillations using RENO and NEOS data, Phys. Rev. D 105 (11) (2022) L111101. arXiv:2011.00896, doi:10.1103/PhysRevD.105.L111101.

[11] H. Almazán, et al., Improved sterile neutrino constraints from the STEREO experiment with 179 days of reactor-on data, Phys. Rev. D 102 (5) (2020) 052002. arXiv:1912.06582, doi:10.1103/PhysRevD.102.052002.

[12] M. Dentler, A. Hernández-Cabezudo, J. Kopp, P. A. N. Machado, M. Maltoni, I. Martinez-Soler, T. Schwetz, Updated Global Analysis of Neutrino Oscillations in the Presence of eV-Scale Sterile Neutrinos, JHEP 08 (2018) 010. arXiv:1803.10661, doi:10.1007/JHEP08(2018)010.

[13] A. Diaz, C. A. Argüelles, G. H. Collin, J. M. Conrad, M. H. Shaevitz, Where Are We With Light Sterile Neutrinos?, Phys. Rept. 884 (2020) 1–59. arXiv:1906.00045, doi:10.1016/j.physrep.2020.08.005.

[14] S. Gariazzo, C. Giunti, M. Laveder, Y. F. Li, Updated Global 3+1 Analysis of Short-BaseLine Neutrino Oscillations, JHEP 06 (2017) 135. arXiv:1703.00860, doi:10.1007/JHEP06(2017)135.

[15] J. M. Hardin, I. Martinez-Soler, A. Diaz, M. Jin, N. W. Kamp, C. A. Argüelles, J. M. Conrad, M. H. Shaevitz, New Clues about light sterile neutrinos: preference for models with damping effects in global fits, JHEP 09 (2023) 058. arXiv:2211.02610, doi:10.1007/JHEP09(2023)058.

[16] E. K. Akhmedov, Neutrino oscillations in inhomogeneous matter. (In Russian), Sov. J. Nucl. Phys. 47 (1988) 301–302.

[17] P. I. Krastev, A. Y. Smirnov, Parametric Effects in Neutrino Oscillations, Phys. Lett. B 226 (1989) 341–346. doi:10.1016/0370-2693(89)91206-9.

[18] M. Chizhov, M. Maris, S. T. Petcov, On the oscillation length resonance in the transitions of solar and atmospheric neutrinos crossing the earth core (7 1998). arXiv:hep-ph/9810501.

[19] M. V. Chizhov, S. T. Petcov, New conditions for a total neutrino conversion in a medium, Phys. Rev. Lett. 83 (1999) 1096–1099. arXiv:hep-ph/9903399, doi:10.1103/PhysRevLett.83.1096.

[20] E. K. Akhmedov, A. Y. Smirnov, Comment on 'New conditions for a total neutrino conversion in a medium', Phys. Rev. Lett. 85 (2000) 3978. arXiv:hep-ph/9910433, doi:10.1103/PhysRevLett.85.3978.

[21] H. Nunokawa, O. L. G. Peres, R. Zukanovich Funchal, Probing the LSND mass scale and four neutrino scenarios with a neutrino telescope, Phys. Lett. B 562 (2003) 279–290. arXiv:hep-ph/0302039, doi:10.1016/S0370-2693(03)00603-8.

[22] M. G. Aartsen, et al., The IceCube Neutrino Observatory: Instrumentation and Online Systems, JINST 12 (03) (2017) P03012. arXiv:1612.05093, doi:10.1088/1748-0221/12/03/P03012.

[23] A. Fedynitch, R. Engel, T. K. Gaisser, F. Riehn, T. Stanev, Calculation of conventional and prompt lepton fluxes at very high energy, EPJ Web Conf. 99 (2015) 08001. arXiv:1503.00544, doi:10.1051/epjconf/20159908001.

[24] M. G. Aartsen, et al., Measurement of the Atmospheric ν_e Spectrum with IceCube, Phys. Rev. D 91 (2015) 122004. arXiv:1504.03753, doi:10.1103/PhysRevD.91.122004.

[25] S. Razzaque, A. Y. Smirnov, Searching for sterile neutrinos in ice, Journal of High Energy Physics 2011 (2011) 84. arXiv:1104.1390, doi:10.1007/JHEP07(2011)084.

[26] A. Esmaili, F. Halzen, O. L. G. Peres, Constraining Sterile Neutrinos with AMANDA and IceCube Atmospheric Neutrino Data, JCAP 11 (2012) 041. arXiv:1206.6903, doi:10.1088/1475-7516/2012/11/041.

[27] A. Esmaili, A. Y. Smirnov, Restricting the LSND and MiniBooNE sterile neutrinos with the IceCube atmospheric neutrino data, JHEP 12 (2013) 014. arXiv:1307.6824, doi:10.1007/JHEP12(2013)014.

[28] M. G. Aartsen, et al., Searches for Sterile Neutrinos with the IceCube Detector, Phys. Rev. Lett. 117 (7) (2016) 071801. arXiv:1605.01990, doi:10.1103/PhysRevLett.117.071801.

[29] M. G. Aartsen, et al., eV-Scale Sterile Neutrino Search Using Eight Years of Atmospheric Muon Neutrino Data from the IceCube Neutrino Observatory, Phys. Rev. Lett. 125 (14) (2020) 141801. arXiv:2005.12942, doi:10.1103/PhysRevLett.125.141801.

[30] M. G. Aartsen, et al., Searching for eV-scale sterile neutrinos with eight years of atmospheric neutrinos at the IceCube Neutrino Telescope, Phys. Rev. D 102 (5) (2020) 052009. arXiv:2005.12943, doi:10.1103/PhysRevD.102.052009.

[31] M. G. Aartsen, et al., Search for sterile neutrino mixing using three years of IceCube DeepCore data, Phys. Rev. D 95 (11) (2017) 112002. arXiv:1702.05160, doi:10.1103/PhysRevD.95.112002.

[32] K. Abe, et al., Limits on sterile neutrino mixing using atmospheric neutrinos in Super-Kamiokande, Phys. Rev. D 91 (2015) 052019. arXiv:1410.2008, doi:10.1103/PhysRevD.91.052019.

[33] K. Abe, et al., Search for light sterile neutrinos with the T2K far detector Super-Kamiokande at a baseline of 295 km, Phys. Rev. D 99 (7) (2019) 071103. arXiv:1902.06529, doi:10.1103/PhysRevD.99.071103.

[34] A. Albert, et al., Measuring the atmospheric neutrino oscillation parameters and constraining the 3+1 neutrino model with ten years of ANTARES data, JHEP 06 (2019) 113. arXiv:1812.08650, doi:10.1007/JHEP06(2019)113.

[35] T. K. Gaisser, Spectrum of cosmic-ray nucleons, kaon production, and the atmospheric muon charge ratio, Astropart. Phys. 35 (2012) 801–806. arXiv:1111.6675, doi:10.1016/j.astropartphys.2012.02.010.

[36] F. Riehn, H. P. Dembinski, R. Engel, A. Fedynitch, T. K. Gaisser, T. Stanev, The hadronic interaction model SIBYLL 2.3c and Feynman scaling, PoS ICRC2017 (2018) 301. arXiv:1709.07227, doi:10.22323/1.301.0301.

[37] Jet Propulsion Laboratory , AIRS/AMSU/HSB Version 6 Level 3 Product User Guide, Version 1.2 (11 2014).

[38] A. Bhattacharya, R. Enberg, M. H. Reno, I. Sarcevic, A. Stasto, Perturbative charm production and the prompt atmospheric neutrino flux in light of RHIC and LHC, JHEP 06 (2015) 110. arXiv:1502.01076, doi:10.1007/JHEP06(2015)110.

[39] R. Abbasi, et al., The IceCube high-energy starting event sample: Description and flux characterization with 7.5 years of data, Phys. Rev. D 104 (2021) 022002. arXiv:2011.03545, doi:10.1103/PhysRevD.104.022002.

[40] M. G. Aartsen, et al., Evidence for High-Energy Extraterrestrial Neutrinos at the IceCube Detector, Science 342 (2013) 1242856. arXiv:1311.5238, doi:10.1126/science.1242856.

[41] M. G. Aartsen, et al., Observation of High-Energy Astrophysical Neutrinos in Three Years of IceCube Data, Phys. Rev. Lett. 113 (2014) 101101. arXiv:1405.5303, doi:10.1103/PhysRevLett.113.101101.

[42] M. G. Aartsen, et al., Observation and Characterization of a Cosmic Muon Neutrino Flux from the Northern Hemisphere using six years of IceCube data, Astrophys. J. 833 (1) (2016) 3. arXiv:1607.08006, doi:10.3847/0004-637X/833/1/3.

[43] M. G. Aartsen, et al., Characteristics of the diffuse astrophysical electron and tau neutrino flux with six years of IceCube high energy cascade data, Phys. Rev. Lett. 125 (12) (2020) 121104. arXiv:2001.09520, doi:10.1103/PhysRevLett.125.121104.

[44] C. A. Argüelles, J. Salvado, C. N. Weaver, nuSQuIDS: A toolbox for neutrino propagation, Comput. Phys. Commun. 277 (2022) 108346. arXiv:2112.13804, doi:10.1016/j.cpc.2022.108346.

[45] I. Esteban, M. C. Gonzalez-Garcia, M. Maltoni, T. Schwetz, A. Zhou, The fate of hints: updated global analysis of three-flavor neutrino oscillations, JHEP 09 (2020) 178. arXiv:2007.14792, doi:10.1007/JHEP09(2020)178.

[46] A. Cooper-Sarkar, P. Mertsch, S. Sarkar, The high energy neutrino cross-section in the Standard Model and its uncertainty, JHEP 08 (2011) 042. arXiv:1106.3723, doi:10.1007/JHEP08(2011)042.

[47] F. Halzen, D. Saltzberg, Tau-neutrino appearance with a 1000 megaparsec baseline, Phys. Rev. Lett. 81 (1998) 4305–4308. arXiv:hep-ph/9804354, doi:10.1103/PhysRevLett.81.4305.

[48] A. M. Dziewonski, D. L. Anderson, Preliminary reference earth model, Phys. Earth Planet. Interiors 25 (1981) 297–356. doi:10.1016/0031-9201(81)90046-7.

[49] M. G. Aartsen, et al., Energy Reconstruction Methods in the IceCube Neutrino Telescope, JINST 9 (2014) P03009. arXiv:1311.4767, doi:10.1088/1748-0221/9/03/P03009.

[50] M. G. Aartsen, et al., Evidence for Astrophysical Muon Neutrinos from the Northern Sky with IceCube, Phys. Rev. Lett. 115 (8) (2015) 081102. arXiv:1507.04005, doi:10.1103/PhysRevLett.115.081102.

[51] R. Abbasi, et al., The IceCube Data Acquisition System: Signal Capture, Digitization, and Timestamping, Nucl. Instrum. Meth. A 601 (2009) 294–316. arXiv:0810.4930, doi:10.1016/j.nima.2009.01.001.

[52] R. Abbasi, et al., The Design and Performance of IceCube DeepCore, As-tropart. Phys. 35 (2012) 615–624. arXiv:1109.6096, doi:10.1016/j.astropartphys.2012.01.004.

[53] R. Abbasi, et al., Search for Unstable Sterile Neutrinos with the IceCube Neutrino Observatory, Phys. Rev. Lett. 129 (15) (2022) 151801. arXiv:2204.00612, doi:10.1103/PhysRevLett.129.151801.

[54] C. Weaver, Evidence for astrophysical muon neutrinos from the northern sky, Ph.D. thesis, Wisconsin U., Madison, Wisconsin U., Madison (2015).

[55] R. Abbasi, et al., LeptonInjector and LeptonWeighter: A neutrino event generator and weighter for neutrino observatories, Comput. Phys. Commun. 266 (2021) 108018. arXiv:2012.10449, doi:10.1016/j.cpc.2021.108018.

[56] J. H. Koehne, K. Frantzen, M. Schmitz, T. Fuchs, W. Rhode, D. Chirkin, J. Becker Tjus, PROPOSAL: A tool for propagation of charged leptons, Comput. Phys. Commun. 184 (2013) 2070–2090. doi:10.1016/j.cpc.2013.04.001.

[57] P. Lipari, S. Vernetto, The shape of the cosmic ray proton spectrum, As-tropart. Phys. 120 (2020) 102441. arXiv:1911.01311, doi:10.1016/j.astropartphys.2020.102441.

[58] G. D. Barr, T. K. Gaisser, S. Robbins, T. Stanev, Uncertainties in Atmospheric Neutrino Fluxes, Phys. Rev. D 74 (2006) 094009. arXiv:astro-ph/0611266, doi:10.1103/PhysRevD.74.094009.

[59] M. G. Aartsen, et al., Efficient propagation of systematic uncertainties from calibration to analysis with the SnowStorm method in Ice-Cube, JCAP 10 (2019) 048. arXiv:1909.01530, doi:10.1088/1475-7516/2019/10/048.

[60] C. A. Argüelles, A. Schneider, T. Yuan, A binned likelihood for stochastic models, JHEP 06 (2019) 030. arXiv:1901.04645, doi:10.1007/JHEP06(2019)030.

[61] F. Feroz, M. P. Hobson, E. Cameron, A. N. Pettitt, Importance Nested Sampling and the MultiNest Algorithm, Open J. Astrophys. 2 (1) (2019) 10. arXiv:1306.2144, doi:10.21105/astro.1306.2144.

[62] H. Jeffreys, The Theory of Probability, Oxford Classic Texts in the Physical Sciences, 1939.

[63] A. Ishihara, The IceCube Upgrade - Design and Science Goals, PoS ICRC2019 (2021) 1031. arXiv:1908.09441, doi:10.22323/1.358.1031.

[64] B. R. Smithers, B. J. P. Jones, C. A. Argüelles, J. M. Conrad, A. Diaz, Cascade appearance signatures of sterile neutrinos at 1–100 TeV, Phys. Rev. D 105 (5) (2022) 052001. arXiv:2111.08722, doi:10.1103/PhysRevD.105.052001.

Appendix A. Systematic parameter effects on event rate

Figure A.7 shows how the expected reconstructed event rate changes when the given systematic parameter is shifted up by 1σ.

Appendix B. Oscillogram at best-fit point

Figure B.8 shows the oscillograms for $\bar{\nu}_\mu \rightarrow \bar{\nu}_\mu$ disappearance and $\bar{\nu}_\mu \rightarrow \bar{\nu}_\tau$ appearance at the best-fit point of $\Delta m^2_{41} = 5.0\,\text{eV}^2$, $|U_{\mu4}|^2 = 0.032$, and $|U_{\tau4}|^2 = 0.010$.

Appendix C. Wilks' vs. frequentist coverage tests

The analysis presents confidence limits based on Wilks' theorem with three degrees of freedom. In order to test the validity of this assumption, frequentist "spot-checks" were performed. In this study, simulations were fit to obtain a sampled $-2\Delta \log \mathcal{L}$ distribution. We report the results in Table C.4, where each column gives the true coverage found through simulations, which should be compared to the coverage at the defined Wilks' theorem confidence levels of 90%, 95% and 99%.
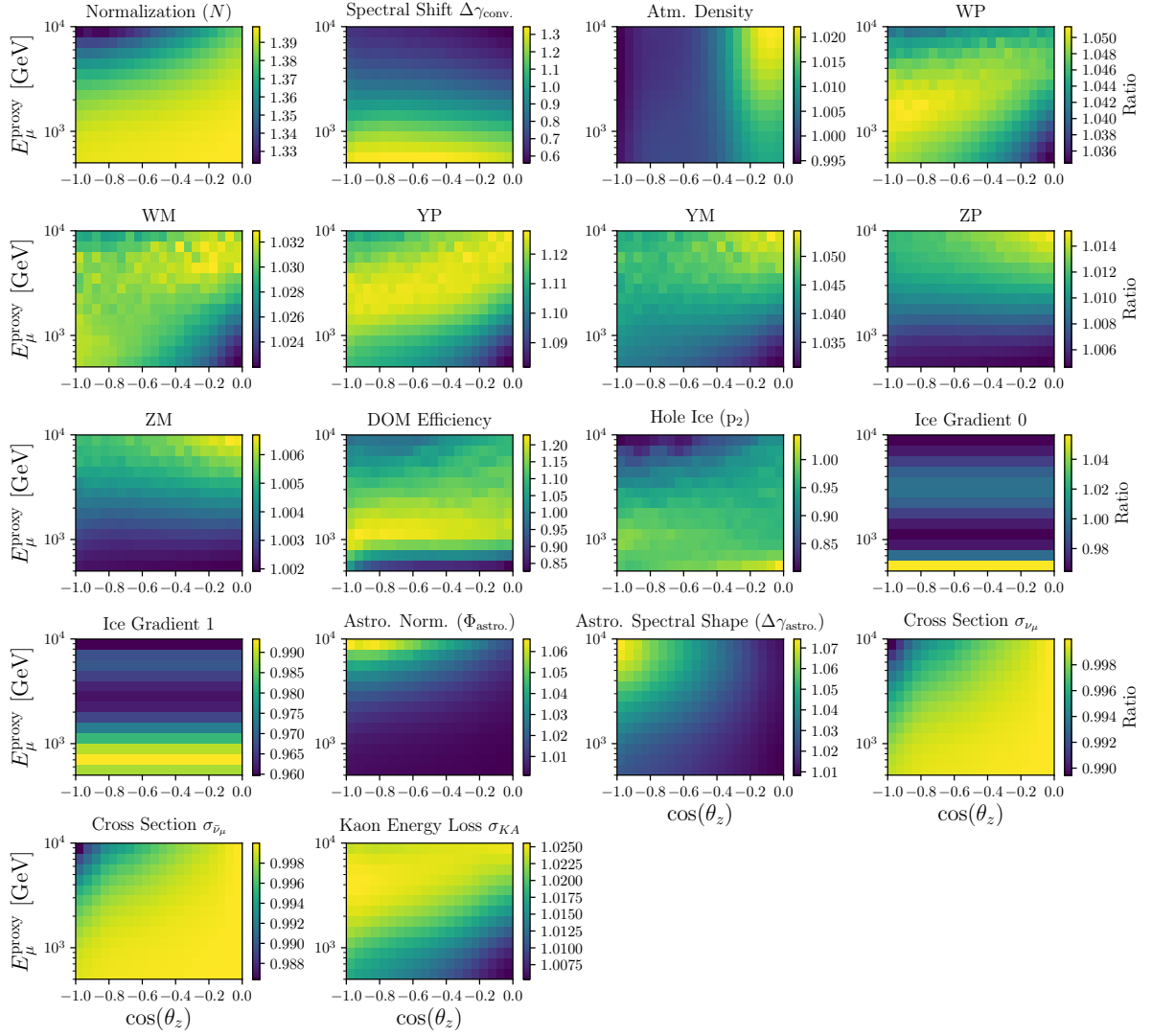
Figure A.7: Each plot shows the ratio of the expected event rate when each systematic parameter is shifted up by 1σ over the expected event rate with nominal systematic parameter values. All plots are made assuming the no sterile neutrino model.

$$\bar{\nu}_\mu \to \bar{\nu}_\mu$$

$$\bar{\nu}_\mu \to \bar{\nu}_\tau$$
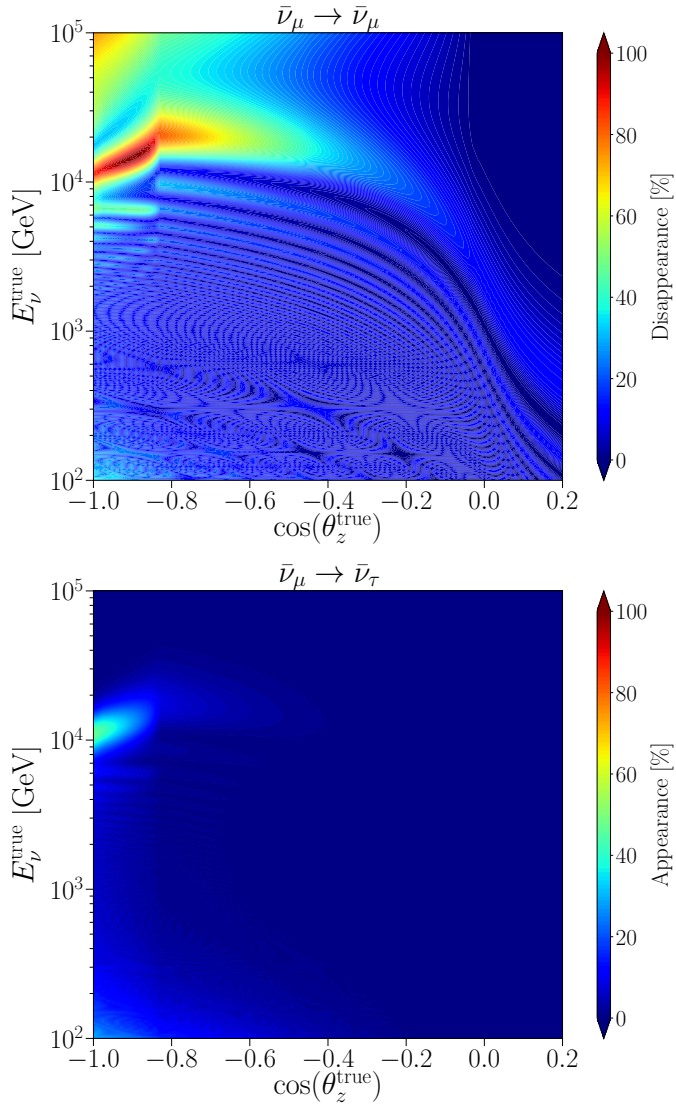
Figure B.8: **Top:** The expected $\bar{\nu}_\mu \to \bar{\nu}_\mu$ disappearance oscillations at the best-fit point of $\Delta m^2_{41} = 5.0 \, \mathrm{eV}^2$, $|U_{\mu4}|^2 = 0.032$, and $|U_{\tau4}|^2 = 0.010$. **Bottom:** The expected $\bar{\nu}_\mu \to \bar{\nu}_\tau$ appearance at the same best-fit point.

Sampled Point	Coverage, assuming Wilks' CL		
$(\Delta m^2_{41}, |U_{\mu4}|^2, |U_{\tau4}|^2)$	90%	95%	99%
$(0, 0, 0)$	$93.9^{+0.8}_{-0.8}\%$	$97.7^{+0.5}_{-0.6}\%$	$99.4^{+0.2}_{-0.4}\%$
$(5, 0.03, 0.01)$	$89.0^{+1.4}_{-1.6}\%$	$95.2^{+1.0}_{-1.2}\%$	$99.6^{+0.3}_{-0.5}\%$
$(1.0, 0.0063, 0.10)$	$93.4^{+1.1}_{-1.3}\%$	$97.4^{+0.7}_{-0.9}\%$	$99.2^{+0.4}_{-0.6}\%$
$(10, 0.16, 0.0016)$	$92.4^{+1.2}_{-1.4}\%$	$96.8^{+0.8}_{-1.0}\%$	$99.6^{+0.3}_{-0.5}\%$

Table C.4: Summary of the Wilk's coverage test at a selection of sampled points.